Bifunctional Strontium Cobalt Molybdenum Oxide (Sr_2CoMoO_6) Perovskite as an Efficient Catalyst for Electrochemical Water Splitting Reactions in Alkaline Media

Shahan Atif[+],[a] Abhisek Padhy[+],*[a] Pawan Kumar Jha,[a] Dorothy Sachdeva,[b] and Prabeer Barpanda*[a, c, d]

Developing earth-abundant low-cost electrocatalysts is of prime research interest towards the need for clean energy technology, such as water-splitting reactions. Herein, we have explored the electrocatalytic activity of the double perovskite-based strontium cobalt molybdenum oxide (SCMO) towards water-splitting reactions, both hydrogen evolution reaction (HER) and oxygen evolution reaction (OER), in harsh alkaline condition (1 M KOH). Prepared by scalable autocombustion synthesis, the as-synthesised bulk SCMO perovskite exhibited impressive electrocatalytic performance attributed to its substantial electrochemical active surface area, measured at 26.3 cm^2. For the OER, it exhibited an overpotential of 350 mV with a Tafel slope value of 76 mV/dec. Concurrently, it showed proficient activity in the HER, revealing an overpotential of 270 mV and a Tafel slope of 112 mV/dec. Further, this perovskite material was stable during continuous electrocatalysis over a 24 h period in harsh alkaline media with a negligible increase in observed overpotential value. The electronic density of states confirmed that the Co plays a pivotal role in enhancing electrocatalytic activities. This is achieved by a substantial reduction in the band gap and enhancement of the *d*-band centre to an optimal level, rendering the system more favourable for electrocatalytic reactions. Our study contributes essential insights to the advancement of the design and utilization of perovskite-based catalysts in the realm of sustainable energy technologies.

Introduction

The challenges linked to the exhaustion of fossil fuels, rapid population growth, greenhouse effect, and climate change can be mitigated through the adoption of various sustainable energy technologies. In this context, hydrogen stands out as a promising alternative to carbonaceous fuel sources.[1] Achieving cost-effective and efficient hydrogen production is feasible through water electrolysis.[2,3] Nonetheless, water electrolysis faces several challenges attributed to the oxygen evolution reaction at the anode warranting a four-electron pathway to complete the catalytic cycle. Therefore, the role of an electrocatalyst becomes crucial in facilitating rapid oxygen evolution kinetics with minimal overpotential. At this juncture, while precious metal-based state-of-the-art electrocatalysts such as RuO_2 and IrO_2 are well-established for anodic oxygen evolution reactions, their limited availability and high-cost restrict their widespread utilization.[4–6] To circumvent this issue, designing and developing electrocatalysts comprising earth-abundant elements via simple and scalable synthetic pathways is crucial to ensure economic viability.

It has triggered active research to develop highly efficient, durable, and cost-effective electrocatalysts. This emphasis signifies research endeavors specifically aimed at exploring and advancing non-precious metal-based alternative catalysts. These include oxides and hydroxides,[7] chalcogenides,[8] borides,[9] and phosphates[10] constituting 3*d* transition metals such as Fe, Co, and Ni. In recent years, perovskite and double perovskite (DP) based oxides have garnered considerable attention owing to their facile synthetic pathways, efficient OER activity, exceptional durability, diverse properties, cost-effectiveness, and abundance in the realm of water electrolysis.[11] The robust metal-oxygen covalency and intrinsic oxygen deficiency in perovskite and double perovskite frameworks contribute significantly to uplift the OER kinetics when compared to novel metal-based catalysts.[12] Numerous studies report improvement in electrocatalytic performance through vacancy modulation,[13] heterostructure engineering,[14] and nanostructuring.[15,16] Chen and co-workers synthesised SnCoFe hydroxide perovskite with Sn vacancies on the surface by energetic plasma etching.[13] The active catalyst (SnCoFe–Ar) projects an overpotential value of 270 mV with a Tafel slope value of 42.3 mV/dec. Karki et al. revealed both the HER and OER activity of the perovskite oxides synthesised by varying the A-site and managing the ordering.

[a] *S. Atif,[+] A. Padhy,[+] P. K. Jha, Dr. P. Barpanda*
Faraday Materials Laboratory (FaMaL), Materials Research Centre, Indian Institute of Science, Bangalore 560012, India,
E-mail: abhisekpadhy@iisc.ac.in
prabeer@iisc.ac.inn

[b] *D. Sachdeva*
Materials Research Centre, Indian Institute of Science, Bangalore 560012, India

[c] *Dr. P. Barpanda*
Helmholtz Institute Ulm (HIU), Electrochemical Energy Storage, Ulm 89081, Germany

[d] *Dr. P. Barpanda*
Institute of Nanotechnology, Karlsruhe Institute of Technology, Karlsruhe 76021, Germany

[+] *Authors contributed equally*

The highly ordered perovskite $Ca_2FeCoO_{6-\delta}$ projects an overpotential value of 250 mV for both HER and OER with a Tafel slope value of 105 mV/dec and 57 mV/dec, respectively.[17] Despite the array of techniques available for enhancing the intrinsic electrochemical activity of perovskite-based materials, the electrochemical active surface area requires careful consideration to enhance catalytic performance for bifunctionality (OER and HER). This can be achieved by adjusting the morphology of the electroactive material through modification in synthetic conditions.

In this study, we have introduced a double perovskite, Sr_2CoMoO_6, synthesized using both solid-state (SS-SCMO) and solution-combustion (SC-SCMO) routes, as an electrocatalyst for both OER and HER activity in harsh alkaline media (1 M KOH). The solution combustion (wet) route led to diminished agglomeration in the product material (SC-SCMO) resulting in an enhanced electrochemical active surface area (ECSA) of 26.3 cm^2. As a consequence, superior bifunctional electrocatalytic (HER and OER) activities were observed in the perovskite product.

Specifically, the SC-SCMO exhibited an overpotential value of 350 mV for OER and 270 mV for HER, which is comparatively lower than that of SS-SCMO, where overpotential values of 410 mV for OER and 420 mV for HER were observed. Additionally, the structure and electrocatalytic activity of this double perovskite was found to be very stable even after 24 h of continuous electrolysis. In congruence with these experimental results, the first principle calculations revealed not just a noteworthy increase in electronic conductivity, but also a significant alteration in the electronic structure, enhancing fast charge transfer kinetics and catalytic (de) adsorption processes. This study underscores the impact of electrochemical active surface area on both the HER and OER electrocatalytic activity. Further, the resilience exhibited during prolonged electrolysis in harsh electrolytic conditions establishes SCMO double perovskite as a robust economic bifunctional electrocatalyst for water splitting application.

Experimental Section

Reagents: strontium nitrate ($Sr(NO_3)_2$, SD Fine Chem., 99%), cobaltous nitrate hexahydrate ($Co(NO_3)_2 \cdot 6H_2O$, SD Fine Chem., 97%), ammonium molybdate tetrahydrate ($(NH_4)_6Mo_7O_{24} \cdot 4H_2O$, SD Fine Chem., 99%), oxalic acid ($C_2H_2O_4$, SD Fine Chem., 99%), cobalt (II,III) oxide (Co_3O_4, SD Fine Chem., 99%), molybdenum oxide (MoO_3, SD Fine Chem., 99%), Super P carbon black (Sigma-Aldrich), ruthenium oxide (RuO_2, Sigma-Aldrich), Pt/C (20 weight%, Sigma-Aldrich) and Nafion (5 wt%, Sigma-Aldrich). Merck Milli-Q water was used throughout the experiments.

Synthesis of Sr_2CoMoO_6

The synthesis of the double perovskite Sr_2CoMoO_6 was conducted through both (dry) solid-state and (wet) solution-combustion methods, as detailed in previous reports,[18,19] with slight modification in the synthetic conditions. For solid-state synthesis, stoichiometric amounts of $Sr(NO_3)_2$ (1.71 gm), MoO_3 (0.58 gm) and Co_3O_4 (0.33 gm) precursors were taken and thoroughly ground with a mortar and pestle. The resultant mixture was pelletised and annealed at 1050 °C for 10 h at the heating rate of 5 °C/min in ambient air without any intermediate grinding. For solution-combustion route, stoichiometric amounts of $Sr(NO_3)_2$ (2.14 gm), $Co(NO_3)_2 \cdot 6H_2O$ (1.5 gm), and $(NH_4)_6Mo_7O_{24} \cdot 4H_2O$ (0.9 gm) were dissolved in a 100 mL solution containing oxalic acid ($C_2H_2O_4$) serving as a combustion fuel. With respect to the metal ion, an equimolar amount of oxalic was employed during the reaction. The surplus water in the solution was evaporated by heating the solution at 120 °C. Upon the formation of gel, the sample was subjected to drying at 400 °C for 4 h, followed by a heat treatment at 600 °C for 2 h to ensure the complete removal of volatile organic components. Final calcination was conducted at 900 °C for 10 h in ambient air (heating rate = 5 °C/min) to yield the desired product phase.

Synthesis of $SrMoO_4$

Concurrently, the impurity phase $SrMoO_4$ (SMO) was synthesised using a solvothermal method as outlined elsewhere.[20] In this solvothermal approach, $Sr(NO_3)_2$ (1.07 gm) and $(NH_4)_6Mo_7O_{24} \cdot 4H_2O$ (0.89 gm) served as the precursors in the molar ratio of 1: 0.14 without undergoing further purification. These precursors were added into a 100 ml. Teflon-lined stainless-steel autoclave containing 20 ml of ethylene glycol and subjected to stirring. During stirring, the pH of the solution is maintained at 9 by adding 4 M NaOH and, subsequently, kept in a preheated electric oven at 160 °C for 12 h (heating rate = 5 °C/min). Following, the autoclave was cooled to room temperature gradually. The resulting solid powder was collected, washed with deionized water and ethanol, and then air-dried at room temperature for further electrochemical studies.

Physical Characterizations

The phase purity and structural characteristics of the synthesized SC-SCMO perovskite were determined using a PANalytical X'Pert Pro X-ray diffractometer (XRD) equipped with Cu Kα source (λ = 1.5406 Å) operating at 40 kV/30 mA. Rietveld analysis, facilitated by the GSAS software with EXPGUI graphical interface, was employed to validate the crystal structure.[21,22] The crystal structures were illustrated using VESTA software.[23] Raman spectra of SCMO and SMO were recorded using a WITec Alpha 300 with an Nd: YAG laser source (excitation wavelength λ = 532 nm). Prior to morphological analysis, gold-sputtering was applied on electronically insulating SCMO powder to ensure electronic conductivity. The size and surface morphology were inspected using a field emission scanning electron microscope (FESEM) (Ultra55, Carl Zeiss AG) equipped with an EDS detector and thermal field emission source (W) operating at 0.1–30 kV. The structure and morphology were further probed using an FEI Tecnai T20 ST transmission electron microscope (TEM) operating at 200 kV, equipped with a double-tilt holder. To prepare the TEM sample, a minimal amount of the sample was dispersed in ethanol, drop-casted onto a carbon-coated copper holey grid, and air-dried for further microscopic analysis. The chemical state and presence of constituent elements were investigated by X-ray photoelectron spectroscopy (XPS) using an AXIS ULTRA DLD (Kratos) unit employing a monochromatic Al Kα 1486.6 eV excitation source. Brunauer-Emmett-Teller (BET) surface area of SC-SCMO, SS-SCMO and SMO were measured with a Quantachrome Autosorb iQ2 unit. Prior to the BET analyses, the samples were subjected to degassing at 353 K under vacuum for a duration of 12 h. Subsequently, the surface area and porosity were measured at 77 K using ultrahigh pure N_2 as the adsorbate.

Electrode Preparation and Electrochemical Measurements

A Biologic SP-300 potentiostat was employed to study the electrocatalytic activities of SC-SCMO, SS-SCMO, SMO and RuO_2 catalysts. The electrodes were assembled in a three-electrode configuration employing active catalyst coated over a glassy carbon electrode (GCE, 0.07 cm^2) as the working electrode, Pt-wire as the counter electrode, and Hg/HgO as the reference electrode. For stability measurements, a catalyst-loaded graphite sheet electrode was employed as the working electrode. Prior to catalyst ink preparation, the materials (SS-SCMO, SC-SCMO and SMO) were thoroughly ground with Super P (a carbon source) in a weight ratio of 3:1. Around 1 mg of this mixture was dispersed in 95 μL of ethanol and 5 μL of Nafion solution and was thoroughly mixed in a bath sonicator to form a homogeneous ink. The working electrode was prepared by drop casting 5 μL of the ink (0.71 mg/cm^2) onto the glassy carbon electrode and was dried at room temperature. The electrochemical activity was studied in a freshly prepared 1 M KOH solution.

All electrochemical measurements were carried out with reference to the Hg/HgO electrode, but presented here with respect to the reversible hydrogen electrode (RHE) as per the equation below:[24]

$$E_{RHE} = E^0_{Hg/HgO} + (0.059 \times pH) + E_{Hg/HgO} \quad (1)$$

where $E^0_{Hg/HgO} = 0.098\ V\ vs.\ SHE$, $E_{Hg/HgO}$ is the potential obtained with respect to Hg/HgO. The double layer capacitance (C_{dl}) was determined by performing cyclic voltammetry in the non-faradaic region at a scan rate of 10–100 mV/s. The electrochemically active surface area (ECSA) was calculated using the equation:[25–27]

$$ECSA\ (in\ cm^2) = \frac{C_{dl}}{C_s} \times A_g \quad (2)$$

where C_{dl} is the double-layer capacitance, and C_S is the specific capacitance of the atomically smooth metal oxide surface in alkaline electrolytic condition (i.e., 0.040 mF/cm^2 in alkaline solution). A_g represents the geometric area of the working electrode (A_g = 0.07 cm^2 for GCE). Electrochemical Impedance Spectroscopy (EIS) was carried out in a frequency sweep ranging from 100 kHz to 10 MHz, with an application of a 5 mV AC voltage amplitude. To assess the catalytic efficacy of SC-SCMO perovskite, chronopotentiometry experiments were conducted at a fixed current density of 10 mA/cm^2.

Mass activity (MA) can be calculated by employing the following equation;

$$MA = J/m \quad (3)$$

where J = current density at an overpotential value of 0.5 V and m = amount of active material loaded over glassy carbon (0.35 mg/cm^2).

Specific activity (MA) can be calculated by employing the following equation;

$$SA = J/(10 \times m \times A_{BET}) \quad (4)$$

$$\text{Turn over frequency (TOF } (S^{-1})) = J \times S/(4 \times 96485 \times n) \quad (5)$$

where J = current density @ η = 0.5 V, S = area of the electrode, 4 is the no. of electron participated in OER process, 96485 = Faraday constant, n = no. of moles of active metal atoms in the active material.

Ex-Situ Analysis

For ex-situ analysis, the catalyst loaded onto a graphite sheet was used as the working electrode. Following the stability test via chronopotentiometry, the post-catalytic sample was used for physicochemical investigations to evaluate its structural and elemental integrity. For post-mortem analysis, any variation in structure, morphology and chemical states were probed by using XRD, electron microscopy (SEM, TEM), and XPS respectively using the same protocol as described earlier.

DFT Calculations

Vienna Ab Initio Simulation Package (VASP) was used to perform Spin-polarized DFT + U calculations with U values for Mo and Co being 6.3 and 3.3 respectively.[28–32] The magnetic moments of both Co and Mo were initialized assuming ferromagnetic ordering. A plane-wave energy cut-off of 520 eV was employed and the Brillouin zone integration was carried out with a Γ-centered k-point grid density 32 k-points per Å. Lattice parameters and atomic coordinates were relaxed without imposing any symmetry constraints, utilizing the conjugate gradient method until the maximum force on atoms reached to |0.01| eV/Å with a total energy convergence criterion of 10^{-5} eV. For calculating the density of states (DOS), the GGA + U relaxed ground state structures were used to perform a single self-consistent calculation using Γ-centered grid with a density 64 k-Points per Å.

Results and Discussion

Phase purity and crystal structure of SC-SCMO were analysed using powder X-ray diffraction (PXRD), and Raman spectroscopy. Rietveld refinement of the PXRD pattern confirmed that SCMO crystallized in a tetragonal crystal system with the space group *I*4/*m* (Figure 1(a)). A small amount (ca. 9%) of SMO impurity (ICSD #99089) was noticed along with the perovskite SCMO product phase (ICSD #17705). The inset of Figure 1(a) schematically illustrates the local atomic arrangement in tetragonal Sr_2CoMoO_6, where [MoO_6] and [CoO_6] octahedral units are arranged alternately along the *c*-direction. The corresponding Raman spectrum showed a broad vibration band at ≈795 cm^{-1} attributed to A_{1g} symmetric stretching in SCMO as depicted in Figure 1(b). The conventional solid-state synthesis also led to the desired perovskite phase (SS-SCMO) with tetragonal structure with minimal SMO impurity (Figure S1a). It is worth noting $SrMoO_4$ (SMO) is a thermodynamically stable phase having tetragonal *scheelite* structure (s.g. $I4_1/a$). The Raman spectra of SS-SCMO and SMO are also presented in ESI (Figure S1b and c).[20,33]

The morphology of as-synthesized SC-SCMO and SS-SCMO were examined using FE-SEM as depicted in Figure 2(a) and (b), respectively. The surface morphology of SC-SCMO revealed a distinct granular pattern with even dispersion and smaller particle dimensions. Conversely, SS-SCMO displayed agglomerated clusters with larger particle sizes compared to SC-SCMO. This difference in morphology also correlates with their final electrocatalytic properties as described later. The high-resolution transmission electron microscopy (HRTEM) images of SC-SCMO [Figure 2(c)] exhibited clearly distinguished fringes at a *d*-spacing of 4.6 Å corresponding to the {101} set of planes at an angle of 110°. The selected area

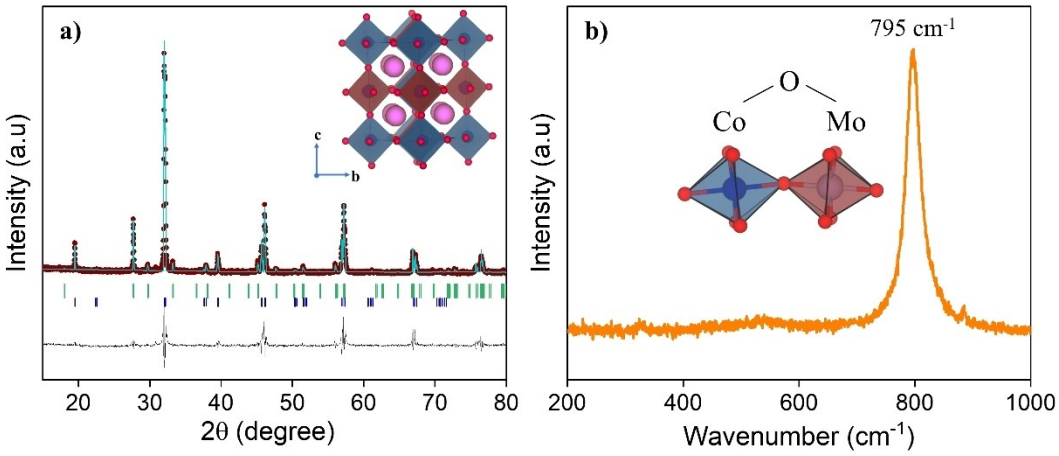

Figure 1. (a) Rietveld refined XRD (λ_{Cu} = 1.5405 Å) pattern of solution combustion prepared perovskite SCMO product. The experimental data points (brown), calculated pattern (cyan), and their difference (black line) are shown. Two phase refinement shows majority of SCMO phase (green Bragg ticks) along with minor (9 wt%) of SMO impurity phase (blue Bragg ticks). (Inset) Corresponding tetragonal crystal structure (space group: *I*4/*m*) projected along the [100] direction. CoO_6 (light blue), MoO_6 octahedra (brown), Sr (pink) and O (red) atoms are shown. (b) Raman spectrum of SCMO perovskite.

electron diffraction (SAED) pattern confirms the crystalline structure of SC-SCMO, with a consistent interplanar distance of 4.6 Å along the [010] zone axis for SC-SCMO [Figure 2(d)] and the [11$\bar{1}$] zone axis for SS-SCMO [Figure S2(b)]. Furthermore, the energy-dispersive X-ray spectroscopy (EDS) mapping confirmed the uniform distribution of constituent Sr, Co, Mo, and O elements in the SC-SCMO product phase with atomic and weight % of Sr (18.75, 44.73), Co (11.25, 16.80), Mo (9.56, 15.16) and O (60.44, 23.21) [Figure 2(e–h)].

To further examine the constituent elements and oxidation states, X-ray photoelectron spectroscopy (XPS) was performed on SC-SCMO. The survey spectrum of SCMO captured all constituent elements (Sr, Co, Mo, and O) [Figure S1(d)]. Deconvolution of the high-resolution XPS spectrum of Co 2*p* resulted in Co $2p_{3/2}$ at 780.2 eV and Co $2p_{1/2}$ at 796 eV, accompanied by two satellite peaks at 783.6 and 801.3 eV, respectively, confirming the +2 oxidation state of Co [Figure 2(i)]. The deconvoluted high-resolution XPS spectrum of Mo indicated peaks ~232 eV and 235.2 eV, corresponding to Mo $3d_{5/2}$ and Mo $3d_{3/2}$, respectively, suggesting the presence of Mo^{6+} ions [Figure 2(j)]. Moreover, the Sr 3*d* peak, as depicted in Figure 2(k), could be resolved into two distinct peaks for Sr $3d_{5/2}$ and Sr $3d_{3/2}$ at binding energy values of 133 eV and 134.7 eV, respectively, indicating the presence of Sr in the +2 oxidation state in the SCMO structure. Figure 2(l) illustrates XPS spectrum of O 1s, which could be deconvoluted into two peaks representing lattice oxygen bonded with cobalt and molybdenum (O^{2-} at 531.3 eV), as well as an adsorbed hydroxide moiety (OH^- at 531.9 eV) present on the perovskite surface.[34]

Following, the electrocatalytic performance of double perovskite SCMO was analysed. The relationship between electrocatalytic activity, synthetic parameters, and morphological attributes was evident in the HER and OER activity. For OER and HER, the sample was drop-casted onto a glassy carbon electrode and was employed as the working electrode. A bare platinum wire and Hg/HgO electrode served as the counter and reference electrodes, respectively. The OER electrocatalysis results in terms of linear sweep voltammetry (LSV) curves for SC-SCMO, SS-SCMO, RuO_2, and SMO (at a sweep rate of 10 mV/s) are shown in Figure 3(a). SC-SCMO exhibited an overpotential value of 350 mV, while SS-SCMO, impurity SMO and the benchmark catalyst RuO_2 displayed overpotential values of 400 mV, 420 mV, and 380 mV, respectively. The overpotential values were calculated at a current density value of 10 mA/cm^2.

Further, the OER kinetics for all samples were examined via Tafel plots (plots of the logarithm of current density against overpotential) derived from the corresponding LSV curves.

As shown in Figure 3(b), SC-SCMO demonstrated a Tafel slope value of 76 mV/dec, approximately two times and 1.5 times lower than those of SS-SCMO (145 mV/dec) and the benchmark catalyst RuO_2 (115 mV/dec), respectively. The lower overpotential and Tafel slope values justify the superior electrocatalytic OER activity of the as-prepared SC-SCMO perovskite. Catalytic stability and surface transformation of the catalyst are crucial factors associated with electrocatalyst stability. After continuous electrolysis for 24 h, SC-SCMO maintained its catalytic activity without significant changes in the chronopotentiometry curve [Figure 3(c)]. Additionally, comparison of the LSV curve for SC-SCMO after 24 hours of electrolysis with the initial LSV revealed similar polarization curve, with minimal (~8 mV) increase in overpotential [Figure 3(d)]. Moreover, for practical applicability, the stability of the catalyst has been evaluated for 3 day (72 h), where minimal change in the overpotential value was observed (Figure S3). It indicates the long term durability of the catalyst after 3 days of electrolysis.

To assess the bifunctional activity of the double perovskite SCMO, it was subjected to electrochemical HER in 1 M KOH electrolyte within a potential window of 0.0 to −0.6 V (vs. RHE). Figure 4(a) illustrates the LSV curves for SMO, SS-SCMO, SC-SCMO, and Pt/C (a benchmark catalyst for HER). Obtaining a current density of 10 mA/cm^2 required an overpotential of 270 mV for SC-SCMO, surpassing the overpotential values of SS-SCMO and SMO. However, the benchmark catalyst Pt/C (with 20% loading) exhibited an overpotential value of 45 mV, showcasing superior catalytic activity compared to SC-SCMO. Nevertheless, the high cost and scarcity of Pt/C limit its widespread application. The kinetics of HER catalysis were evaluated from Tafel slopes, as depicted in Figure 4(b). Tafel

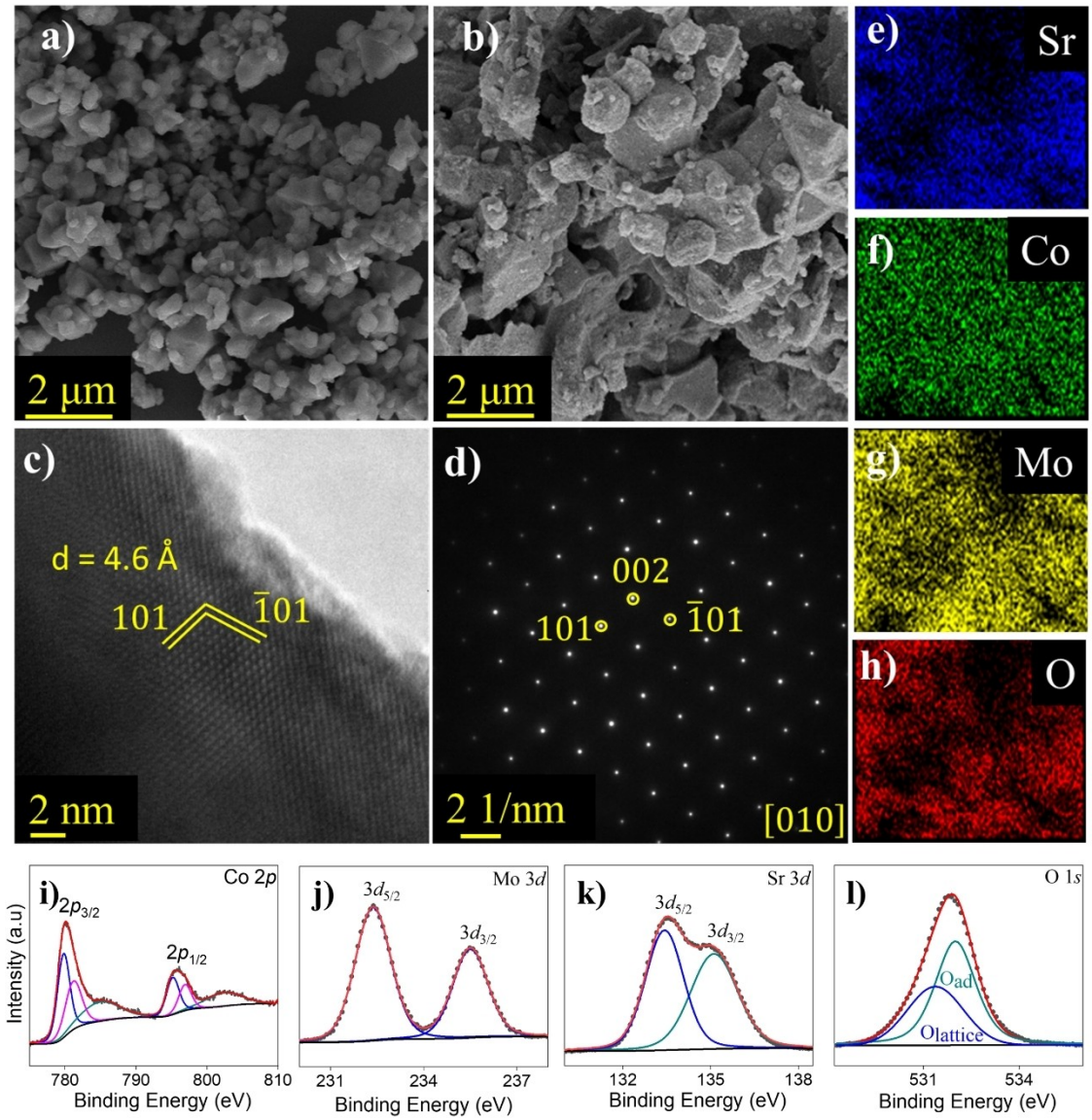

Figure 2. SEM images of SCMO product phase synthesised by (a) solution combustion (SC-SCMO) and (b) solid-state technique (SS-SCMO). (c) HRTEM image and (d) SAED pattern of SC-SCMO. (e–h) Representative elemental mapping of SC-SCMO having a uniform distribution of all constituent elements (Sr, Co, Mo, O). High-resolution XPS spectra corresponding to (i) Co 2*p*, (j) Mo 3*d*, (k) Sr 3*d* spectra and (l) O 1*s*.

slope values of 58 mV/dec, 112 mV/dec, 176 mV/dec, and 65 mV/dec were observed for Pt/C, SC-SCMO, SS-SCMO, and SMO, respectively. Finally, the durability of SC-SCMO in HER electrocatalysis was assessed through a chronopotentiometry stability test lasting for 22 h at a current density of 10 mA/cm^2 showing no significant change in the stability curve (Figure S4a). After 22 hours of HER electrolysis, LSV revealed similar polarization curve, with slight increase in overpotential (Figure S4b).

The enhancement in electrocatalytic activity can be linked to the electrochemically active surface area (ECSA). Cyclic voltammetry (CV) curves in the non-Faradaic region were utilized to assess the ECSA, as depicted in Figure 5(a,b) as well as Figure S5. From these CV curves, the double-layer capacitance (C_{dl}) was determined by plotting capacitive current densities against scan rates [Figure 5(c)]. The calculated C_{dl} values were 15 mF/cm^2 and 1.68 mF/cm^2 for SC-SCMO and SS-SCMO, respectively. Figure 5(d) illustrates the ECSA values of SC-SCMO, RuO_2, SS-SCMO, and SMO. The highest ECSA value of 26.3 cm^2 was observed for SC-SCMO suggesting exposure to an increased number of active sites towards electrolytes contributes to the enhanced electrocatalytic activity of SC-SCMO perovskite. This is further supported by the fact that the BET surface area of SC-SCMO is the highest (ca. 5.87 m^2/g) and is in good agreement with the ECSA of SC-SCMO, indicating a correlation between the accessible surface area and the number of electroactive catalytic sites (Figure S6). Additionally, the improved electrochemical performance of SC-SCMO can be correlated with the charge transfer resistance, as suggested by electrochemical impedance spectroscopy (EIS) in Figure S7. The Nyquist impedance plot is fitted with the corresponding equivalent circuit diagram indicating the lower charge transfer resistance of SC-SCMO (Table S1)

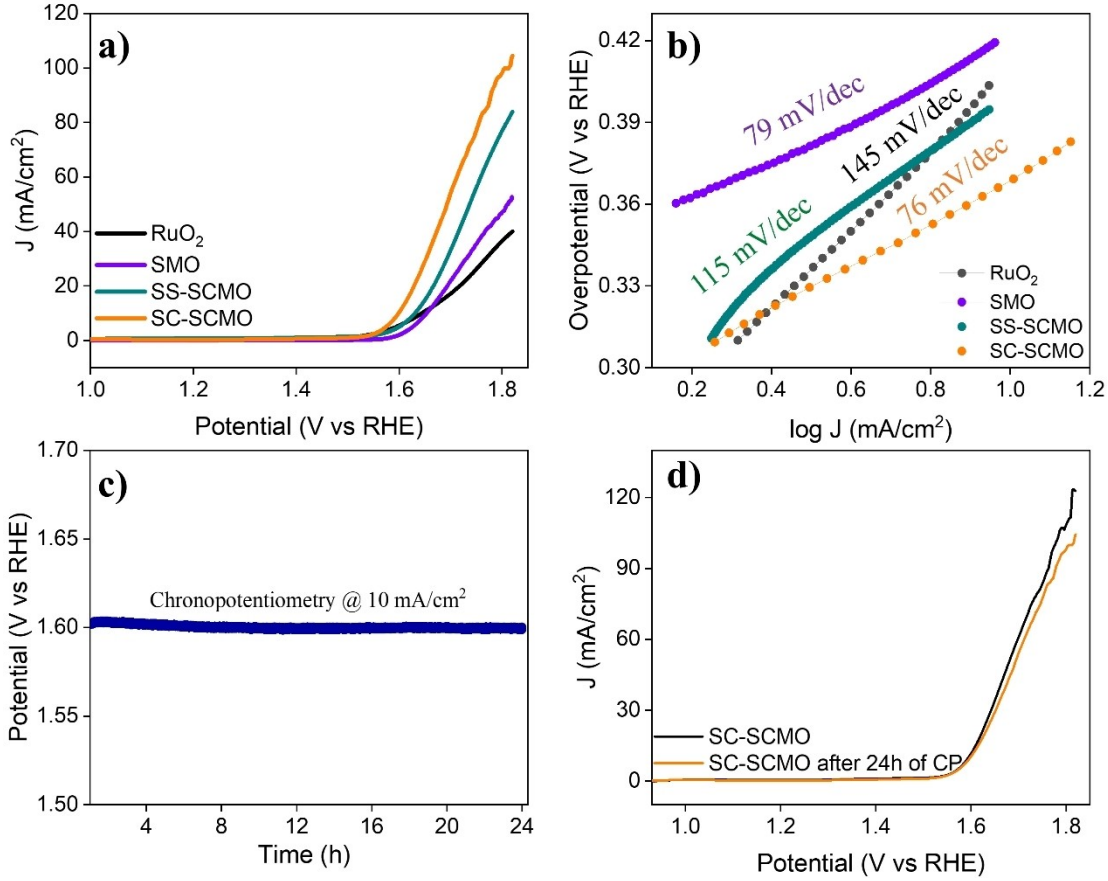

Figure 3. OER performance. (a) Comparative LSV plots of SC-SCMO, SS-SCMO, SMO catalysts and state-of-art RuO_2 in 1 M KOH electrolyte, (b) Tafel plots of all the representative catalysts. (c) Chronopotentiometry stability curve of SC-SCMO for 24 h at a current density of 10 mA/cm^2, and (d) LSV plots for SC-SCMO catalyst before and after chronopotentiometry experiment run for 24 h.

compared to SMO (the impurity) and SS-SCMO. Consequently, the combination of the highest ECSA and the lowest impedance value facilitates superior electrocatalytic performance in SC-SCMO towards both HER and OER activity.

To investigate the electrocatalytic activity at electronic level, the electronic projected density of state (pDOS) for $SrMoO_4$ and Sr_2CoMoO_6 was computed as illustrated in Figure 6. Table S1 compares the GGA+U relaxed and Rietveld refined lattice parameters. The calculated pDOS indicated that both compounds exhibit semiconducting electronic structures, with predicted band gap of 4.23 eV and narrower 1.15 eV in case of SMO and SCMO, respectively. In addition, the nature of valence and conduction

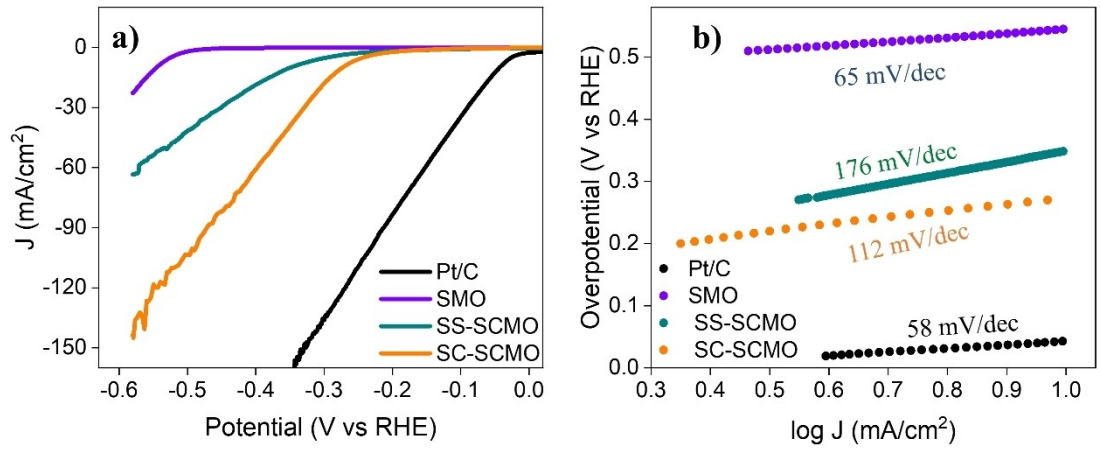

Figure 4. HER performance. (a) Comparative LSV plots of SC-SCMO, SS-SCMO, SMO catalysts and state-of-art Pt/C in 1 M KOH electrolyte. (b) Corresponding Tafel plots of all catalysts.

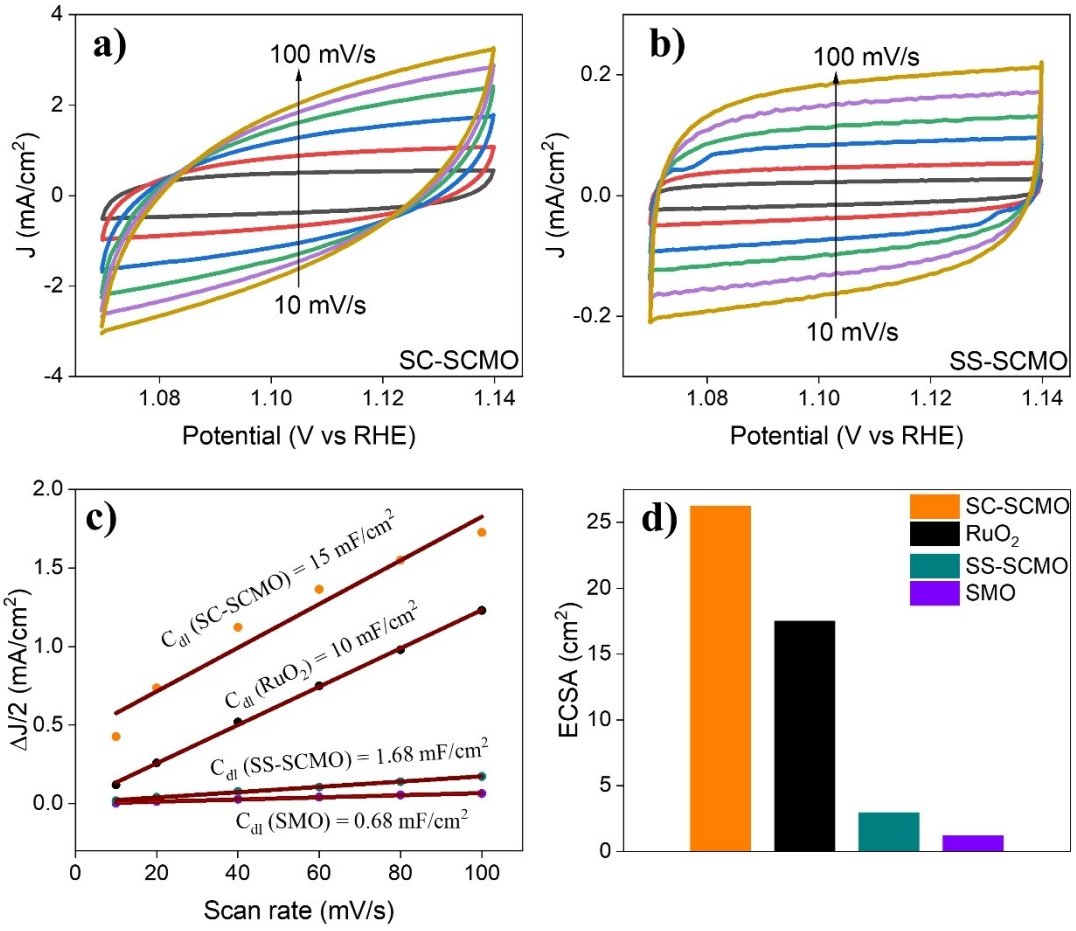

Figure 5. Cyclic voltammograms at different scan rates in the non-Faradaic region for (a) SC-SCMO, (b) SS-SCMO, (c) Plot of cathodic current against scan rate for SC-SCMO, RuO_2, SS-SCMO, and SMO, (d) comparative ECSA values (in cm^2) for SC-SCMO, RuO_2, SS-SCMO, and SMO.

bands changes significantly with the incorporation of Co in SMO compound. In SCMO, The Co 3*d* states dominates near the valence band edge (VBE) while the Mo 4*d* states reside considerably below the VBE. On the other hand, in case of SMO, O 2*p* states dominate near the Fermi level. The narrower band gap of SCMO facilitates swift electron transfer compared to SMO, which exhibits a larger

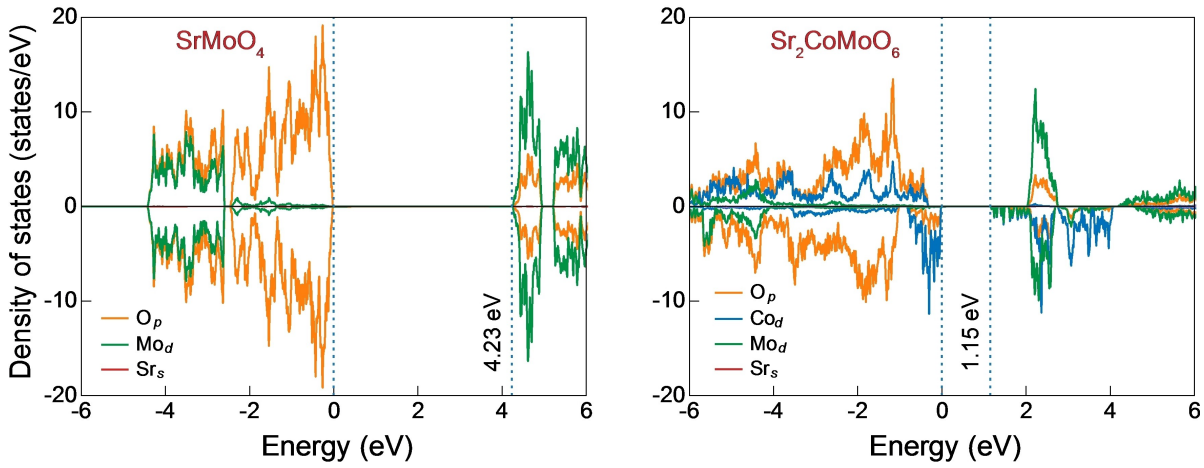

Figure 6. GGA + U-calculated pDOS for (a) $SrMoO_4$ (SMO) and (b) Sr_2MoCoO_6 (SCMO) Blue, orange, green, and red curves correspond to Co *d*, O *p*, Mo *d*, and Sr *s* states, respectively. Positive and negative values of pDOS correspond to the up and down spin electrons, respectively. Dotted blue lines represent the valence and conduction band edges, with the numbers indicating band gap values. The zero on the x-axis is referenced to the valence band maximum or the Fermi level.

band gap. Moreover, the metal *d* band center in SCMO is at a higher energy state compared to SMO, enabling enhanced bonding interactions between the metal *d* states and the adsorbate-related states (*s* and *p* orbitals). From an energetic perspective, the behaviour of electronic bands near the Fermi level plays a crucial role in redox processes. Specifically, bands located at the valence band edge (VBE) or Fermi level can donate electrons to antibonding orbitals of adsorbate species to bind at the surface. 1–3 Further, during the catalysis process, the adsorbed species forms intermediate states during HER and OER reactions. Moreover, the kinetics of this reaction depend on the electronic conductivity/band gap. In the current study, the incorporation of Co significantly reduced the band gap, which leads to facile chemical bond formation between an adsorbate valence level and the d-states of a transition metal at the surface for further reaction steps. Notably, the Co-3*d* band predominantly contributes near the Fermi level, suggesting their active participation in catalysis processes and enhancing overall catalytic activity and stability.[35–37] This leads to the improved electrochemical performance in SCMO, aligning with the experimentally observed superior electrocatalytic performance.

Post-Mortem Analysis

The double perovskite Sr_2CoMoO_6 can be used as a bifunctional electrocatalyst exhibiting both OER and HER activity. It stands out for its ability to be utilized in the bulk form, eliminating the necessity for nanofabrication or composite preparation. The structural and chemical integrity of SCMO catalyst was probed to gauge its operational stability. Notably, SCMO maintains its structural integrity throughout, as evidenced by its characteristic peaks, while additional peaks observed suggest the formation of CoOOH, as indicated by X-ray diffraction data before and after electrocatalysis [Figure 7(a)]. Any possible variation in the morphology, structure and valence states of Co and Mo for the most efficient catalyst SC-SCMO was gauged both before and after electrocatalysis using FESEM (Figure S8), TEM and XPS measurements. The slight change in the morphology is mainly due to the long term electrolysis (72 h) in harsh alkaline media. High-resolution TEM images in Figure 7(b) of post OER samples confirmed the crystalline nature of SC-SCMO even after prolonged electrocatalysis along with the formation of the new phase CoOOH observed from the HRTEM study. Corresponding SAED patterns of SC-SCMO and CoOOH depicted in Figure 7(c) further suggests the in-situ formation of CoOOH during electrolysis for 24 h. Despite these alterations, TEM analyses revealed the presence of SC-SCMO along with CoOOH. The high-resolution XPS spectra of Co 2*p* post-OER electrolysis validated the presence of both the +3 and +2 oxidation states, further substantiating CoOOH formation during OER electrolysis (Figure 7d). In contrast, Mo 3*d* and Sr 3*d* spectra remain unaltered. The O 1s spectra were fitted into three peaks, corresponding to lattice oxygen, oxygen of metal hydroxide bond and an adsorbed oxygen. Similarly, the surface chemical state of SC-SCMO after long term HER was observed from XPS analysis with consistency of the peaks position before and after HER (Figure S9). These post-mortem studies following OER electrolysis indicate the structural integrity of the catalyst, emphasizing its robustness and catalytic efficiency during the electrocatalytic processes. The Raman spectra for the samples after the OER stability test results in the presence of CoOOH (506 and 607 cm^{-1}) along with cobalt oxide (Co_3O_4) as presented in Figure S10.[38]

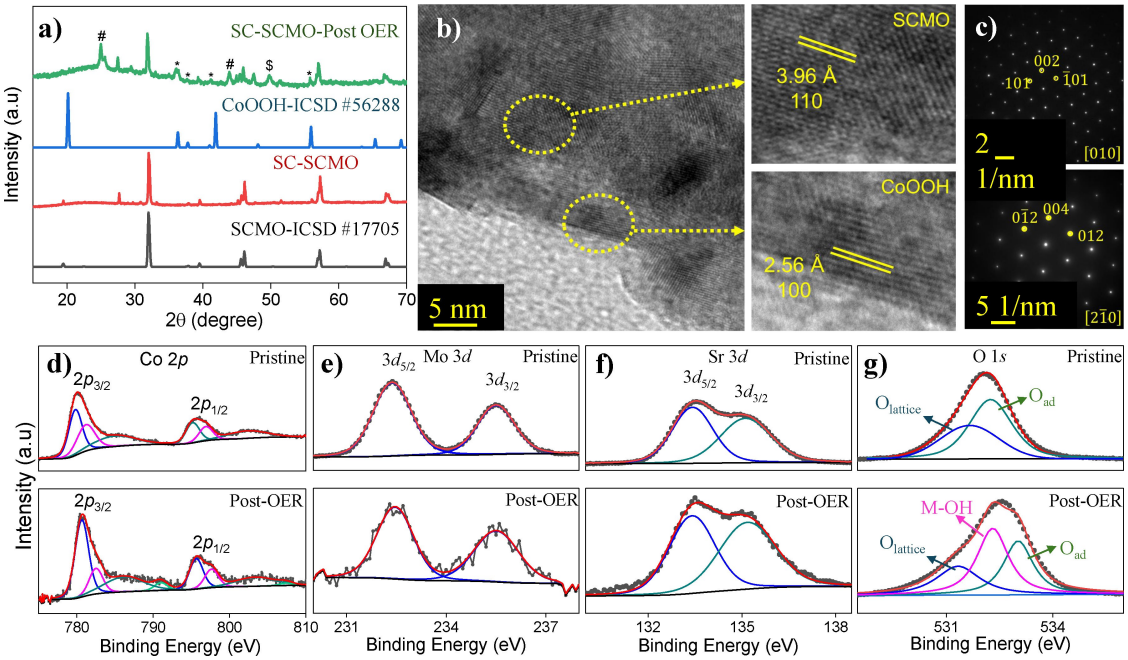

Figure 7. Post-mortem analysis of the SCMO perovskite OER catalyst. (a) Comparative XRD patterns pre and post OER chronopotentiometry experiment. The reference patterns of SCMO and CoOOH are provided. The secondary phases in post OER sample are assigned [# = carbon, * = CoOOH, $ = MoO_3]. (b) HR-TEM, and (c) SAED patterns of pristine and post OER SC-SCMO samples showing the in-situ formation of CoOOH. High resolution XPS spectra before and after OER chronopotentiometry experiment showing the (d) Co 2*p* spectra, (e) Mo 3*d* spectra, (f) Sr 3*d* spectra, and (g) O 1s spectra.

Conclusions

In summary, Sr_2CoMoO_6 double perovskite was successfully synthesised using solution-combustion and solid-state methods. Prepared by scalable solution combustion route, SC-SCMO exhibited efficient bifunctional electrocatalytic activities for both OER and HER reactions for water electrolysis. This catalytic activity can be attributed to the homogeneous morphology, small particle size, and large electrochemical active surface area (ECSA) of SC-SCMO. This perovskite (SCMO) catalyses both OER and HER effectively without any nanofabrication or composite formation. Remarkably, the bifunctional performance of solution-combustion-synthesized SCMO surpasses that of previously reported perovskites and noble-metal electrocatalysts (Table S2). Moreover, the stability tests in alkaline solutions affirm the robust durability of these materials, positioning them as promising candidates for bifunctional electrocatalysts in water electrolysis. This study not only introduces surface area tuning to enhance the bifunctional electrocatalytic activities of perovskites, but also underscores the efficacy of the synthesis approach for preparing perovskite catalysts. These findings provide insights into advancing the design and application of perovskite-based catalysts for sustainable energy technologies.

Acknowledgements

The authors thank the Department of Science and Technology (DST, Government of India) for financial support (CRG/2022/000963). S. A. and D. S. thank Prime Minister Research Fellowships from the Ministry of Human Resource Development (MHRD, Government of India). A. P. is grateful to Indian Institute of Science for an Institute of Eminence postdoctoral fellowship (R(HR)(IoE-IISc)(PDF)(MRC)(80010824)-3101). P. K. J. is grateful to the MHRD for financial assistance. P. B. acknowledges the Alexander von Humboldt Foundation (Bonn, Germany) for a 2022 Humboldt fellowship for experienced researchers.

Conflict of Interests

The authors declare no conflict of interest.

Data Availability Statement

The data that support the findings of this study are available from the corresponding author upon reasonable request.

Keywords: bifunctional electrocatalyst · Hydrogen evolution reaction · Oxygen evolution reaction · perovskite · Water splitting

[1] I. Katsounaros, S. Cherevko, A. R. Zeradjanin, K. J. J. Mayrhofer, *Angew. Chem. Int. Ed.* **2014**, *53*, 102–121.
[2] N. T. Suen, S. F. Hung, Q. Quan, N. Zhang, Y. J. Xu, H. M. Chen, *Chem. Soc. Rev.* **2017**, *46*, 337–365.
[3] L. Han, S. Dong, E. Wang, *Adv. Mater.* **2016**, *28*, 9266–9291.
[4] Y. Lee, J. Suntivich, K. J. May, E. E. Perry, Y. Shao-Horn, *J. Phys. Chem. Lett.* **2012**, *3*, 399–404.
[5] P. Li, Z. Jin, D. Xiao, *J. Mater. Chem. A* **2014**, *2*, 18420–18427.
[6] J. D. Blakemore, N. D. Schley, D. Balcells, J. F. Hull, G. W. Olack, C. D. Incarvito, O. Eisenstein, G. W. Brudvig, R. H. Crabtree, *J. Am. Chem. Soc.* **2010**, *132*, 16017–16029.
[7] Z. Chen, Q. Fan, J. Zhou, X. Wang, M. Huang, H. Jiang, H. Cölfen, *Angew. Chem. Int. Ed.* **2023**, *62*, DOI 10.1002/anie.202309293.
[8] J. Li, F. Xu, K. Wang, J. He, Y. Wang, L. Lei, M. Zhu, L. Zhuang, Z. Xu, *Chem. Eng. Sci.* **2023**, *267*, 118366.
[9] R. K. Tripathy, A. K. Samantara, J. N. Behera, *Dalton Trans.* **2022**, *51*, 2782–2788.
[10] A. Padhy, A. K. Samantara, J. N. Behera, *Sustain. Energy Fuels* **2021**, *5*, 3729–3736.
[11] Y. Zhu, W. Zhou, J. Yu, Y. Chen, M. Liu, Z. Shao, *Chem. Mater.* **2016**, *28*, 1691–1697.
[12] J. Suntivich, K. J. May, H. A. Gasteiger, J. B. Goodenough, Y. Shao-Horn, *Science (1979)* **2011**, *334*, 1383–1385.
[13] D. Chen, M. Qiao, Y. Lu, L. Hao, D. Liu, C. Dong, Y. Li, S. Wang, *Angew. Chem. Int. Ed.* **2018**, *57*, 8691–8696.
[14] Y. Bu, H. Jang, O. Gwon, S. H. Kim, S. H. Joo, G. Nam, S. Kim, Y. Qin, Q. Zhong, S. K. Kwak, J. Cho, G. Kim, *J. Mater. Chem. A* **2019**, *7*, 2048–2054.
[15] J. Jung, H. Y. Jeong, M. G. Kim, G. Nam, J. Park, J. Cho, *Adv. Mater.* **2015**, *27*, 266–271.
[16] S. Li, X. Hao, A. Abudula, G. Guan, *J. Mater. Chem. A* **2019**, *7*, 18674–18707.
[17] S. B. Karki, R. K. Hona, M. Yu, F. Ramezanipour, *ACS Catal.* **2022**, *12*, 10333–10337.
[18] V. V. Sereda, D. S. Tsvetkov, A. L. Sednev, A. I. Druzhinina, D. A. Malyshkin, A. Yu Zuev, *Phys. Chem. Chem. Phys.* **2018**, *20*, 20108–20116.
[19] A. K. Tomar, A. Joshi, S. Atri, G. Singh, R. K. Sharma, *ACS Appl. Mater. Interfaces* **2020**, *12*, 15128–15137.
[20] J. Bi, L. Wu, Y. Zhang, Z. Li, J. Li, X. Fu, *Appl. Catal. B* **2009**, *91*, 135–143.
[21] H. M. Rietveld, *J. Appl. Crystallogr.* **1969**, *2*, 65–71.
[22] B. H. Toby, *J. Appl. Crystallogr.* **2001**, *34*, 210–213.
[23] K. Momma, F. Izumi, *J. Appl. Crystallogr.* **2011**, *44*, 1272–1276.
[24] S. Anantharaj, P. N. Reddy, S. Kundu, *Inorg. Chem.* **2017**, *56*, 1742–1756.
[25] C. C. L. McCrory, S. Jung, J. C. Peters, T. F. Jaramillo, *J. Am. Chem. Soc.* **2013**, *135*, 16977–16987.
[26] D. M. Morales, M. Risch, *J. Phys. Energy* **2021**, *3*, 034013.
[27] H. R. Devi, O. Y. Bisen, Z. Chen, K. K. Nanda, *Chem. Eng. J.* **2022**, *433*, 133649.
[28] G. Kresse, J. Furthmüller, *Phys. Rev. B* **1996**, *54*, 11169–11186.
[29] G. Kresse, J. Hafner, *Phys. Rev. B* **1993**, *47*, 558–561.
[30] G. Kresse, D. Joubert, *Phys. Rev. B* **1999**, *59*, 1758–1775.
[31] J. P. Perdew, K. Burke, M. Ernzerhof, *Phys. Rev. Lett.* **1998**, *80*, 891–891.
[32] V. I. Anisimov, J. Zaanen, O. K. Andersen, *Phys. Rev. B* **1991**, *44*, 943–954.
[33] J. C. Sczancoski, L. S. Cavalcante, M. R. Joya, J. A. Varela, P. S. Pizani, E. Longo, *Chem. Eng. J.* **2008**, *140*, 632–637.
[34] Z. Wang, C. Jin, J. Sui, C. Li, R. Yang, *Int. J. Hydrogen Energy* **2018**, *43*, 20727–20733.
[35] B. Hammer, J. K. Nørskov, *Surf. Sci.* **1995**, *343*, 211–220.
[36] P. Kratzer, B. Hammer, J. K. Nørskov, *Surf. Sci.* **1996**, *359*, 45–53.
[37] J. K. Nørskov, F. Abild-Pedersen, F. Studt, T. Bligaard, *PNAS* **2011**, *108*, 937–943.
[38] A. Moysiadou, S. Lee, C.-S. Hsu, H. M. Chen, X. Hu, *J. Am. Chem. Soc.* **2020**, *142*, 11901–11914.